Damage Localization in a CFRP Beam via Modal Frequency Shifts and Nearest Neighbor Classification

Ömer Dehan Özboz[1], Özkan Altay[2], Murat Özbayoğlu[3], and Özgür Ünver[4]

[1,3,4] *TOBB ETÜ University of Economics and Technology, Ankara, 06560, Turkey*
o.ozboz@etu.edu.tr
mozbayoglu@etu.edu.tr
hounver@etu.edu.tr

[2] *TURKISH AEROSPACE, Ankara, 06980, Turkey*
ozaltay@tai.com.tr

ABSTRACT

Vibration-Based Structural Health Monitoring (SHM) systems offer significant potential for damage detection due to their non-destructive nature and real-time capabilities, while reducing maintenance costs for aerospace and automotive applications. This study investigates the effect of damage on the modal parameters of a Carbon Fiber Reinforced Polymer (CFRP) fixed-free beam, with the goal of identifying damage location and severity. The lamina material properties of the CFRP were evaluated using composite lamination theory (CLT). By altering the location and depth of the damage, numerical analyses were conducted on the CFRP beam, and discrepancies between the intact and damaged models were examined. Modal frequency shifts were quantified using Relative Natural Frequency Change (RNFC), and RNFC-based mapping surfaces dependent on damage location and severity were generated for first four transverse vibrational modes of the beam. The model was validated through experiments on the intact and damaged CFRP specimens. The beam was excited with an impact hammer near the fixed-end, and responses were collected by piezoelectric sensors placed along the beam and laser vibrometer focused at the free end of the beam. The modal parameters were extracted using Eigensystem Realization Algortihm (ERA), a reduced-order system identification method, and the experimental RNFC results of damaged samples were calculated. Finally, Nearest Neighbor search algorithm was employed to estimate the damage location and severity by comparing experimental results to generated RNFC-based mapping surfaces.

1. INTRODUCTION

Structural Health Monitoring systems are employed to assess the integrity and performance of structures throughout their service life. Accurate assessment of a structure's current condition is critical, as it enables early detection of potential issues and helps prevent premature failure, ensuring safety and reducing maintenance costs.

Non-destructive assessment of a structure's condition can be performed using various techniques, including ultrasonic methods, acoustic methods, and strain- or vibration-based approaches. Among these, vibration-based methods are widely studied due to their ability to provide global information about structural integrity. These methods can be further classified based on the specific modal parameters they evaluate, such as natural frequencies, mode shapes, modal slopes, modal curvatures, strain energy, and damping characteristics. Among these parameters, natural frequencies are particularly attractive due to their ease of extraction from measured response data and their sensitivity to global stiffness changes as pointed out by (Sause & Jasiūnienė, 2021).

Relative Natural Frequency Change (RNFC) is one of the methods commonly used to quantify shifts in natural frequencies due to structural damage. The characteristics of RNFC curves with respect to damage location and severity have been investigated in previous studies, such as those by (Gillich & Praisach, 2014) and (Sha, Radzieński, Cao, & Ostachowicz, 2019), under various boundary conditions. These studies also highlight the correlation between RNFC curves and the curvature of mode shapes, emphasizing the physical basis of RNFC as a damage-sensitive metric. (Zhang, Shankar, Ray, Morozov, & Tahtali, 2013) numerically investigated the effect of delamination in composite beam, while (Dahak, Touat, & Kharoubi, 2019) used undamaged curvature mode shapes to relate damage parameters to the frequency shifts.

Various data-driven approaches such as pattern recognition, neural networks, and genetic algorithms have been summarized by (Yan, Cheng, Wu, & Yam, 2007) for structural damage identification. (Abasi, Harsij, & Soraghi, 2021) explored the use of the Nearest Neighbor (NN) algorithm to predict damage characteristics in three-dimensional frame structures.

In this study, a fixed-free Carbon Fiber Reinforced Polymer (CFRP) beam is investigated using RNFC surfaces, with experimental validation performed through NN algorithm.

2. METHODOLOGY

The influence of damage parameters (location and severity) on the first four natural frequencies of a fixed-free beam is investigated through numerical simulations. Finite element analyses are conducted in ABAQUS for various damage scenarios. By comparing the natural frequencies of intact and damaged models, the RNFC is computed for each case to quantify the effect of damage. Based on the results, RNFC surfaces corresponding to the first four vibration modes are constructed to represent the relationship between damage parameters and frequency shifts. Experimental validation is carried out by testing intact and damaged CFRP beam specimens. An impact hammer is used as the excitation source, while responses are measured using piezoelectric sensors and a laser vibrometer. The resulting signals are analyzed using ERA to extract modal parameters. The frequency shifts observed in the experimental data are quantified using the RNFC formulation. These RNFC values are compared with the numerically generated RNFC surfaces using the NN algorithm to estimate the most likely damage parameters.

2.1. Numerical models

The numerical analyses are performed using the ABAQUS finite element software. The composite lay-up feature of the software is utilized to define the material properties, as presented in Table 1. In the table, E_1, E_2, and E_3 represent the longitudinal and transverse Young's moduli, respectively. Direction 1 corresponds to the fiber direction, direction 2 is perpendicular to the fiber direction within the lamina plane, and direction 3 is perpendicular to both the fiber direction and the lamina plane. The parameters ν_{12}, ν_{13}, and ν_{23} denote Poisson's ratios in the orthogonal directions of the lamina, while G_{12}, G_{13}, and G_{23} are the corresponding shear moduli. ρ_c represents the density of the composite.

Table 1. CFRP material properties.

Material Properties					
Fiber Orientation:			$[0/90/0/90]_s$		
E_1	GPa	141.333	G_{12}=G_{13}	GPa	4.743
E_2=E_3	GPa	15.448	G_{23}	GPa	1.231
ρ_c	kg/m^3	1508.3	ν_{12}=ν_{13}=ν_{23}		0.3

The CFRP specimens are manufactured using the vacuum infusion method, and the amount of material used is recorded during production. Assuming a void-free composite, the fiber volume fraction of 0.58 is obtained, and the the material properties are derived using Classical Laminate Theory (CLT). For the estimation of the transverse modulus (E_2) and the in-plane shear modulus (G_{12}), the Halpin–Tsai semi-empirical model is employed (Kaw, 2005).

In the experiments, damage is introduced by removing material from the beam. To ensure consistency between experimental and numerical models, the finite element models are constructed as illustrated in Figure 1, where *l*, *w*, and *t* represent the length, width, and thickness of the beam, respectively. *x* denotes the damage location, d_1 the damage depth, and d_2 the damage thickness. The geometrical dimensions used in the analyses are provided in Table 2. A total of 312 damage scenarios are investigated by varying the damage parameters: 39 different damage locations and 8 different damage depths.

The first four natural frequencies of the intact model are calculated as 19.981, 124.86, 348.01, and 677.47 Hz, as presented in Table 3. For each of the 312 damage cases, the first four natural frequencies are also computed, and the frequency shifts relative to the intact model are quantified using the RNFC, as defined in Eq. (1). In the equation, *k* denotes the k^{th} vibration mode of the beam.

$$RNFC_k = \frac{f_{k\,Damaged} - f_{k\,Intact}}{f_{k\,Intact}} 100\% \qquad (1)$$

The calculated RNFC values are expressed as functions of twice of damage depth (d_1)-since damage is applied on both side of the beam- and normalized damage location ($x_{normalized}$), where 0 corresponds to the fixed end and 1 to the free end of the beam. These results are illustrated in Figure 2 for the first four modes. As shown in the figure, the effect of damage location, varies across different modes. For example, at $x_{normalized} = 0.2$, the second mode is almost unaffected. This is because that location corresponds to a nodal point of the second mode's curvature shape, where the curvature is nearly zero. As a result, no significant dynamical bending moment related to the second mode is induced, and the natural frequency remains largely unchanged for that mode. Since the locations where the curvature is zero vary

Table 2. Dimensions.

Beam dimensions		**Damage dimensions**	
l	40 cm	*x*	[1:39, 1] cm
w	5 cm	$2d_1$	[0:2, 0.25] cm
t	2.4 cm	d_2	0.2 cm

Table 3. Natural frequencies of the intact beam

First four natural frequencies of the beam			
Mode 1	f_1 = 19.981 Hz	**Mode 3**	f_3 = 348.01 Hz
Mode 2	f_2 = 124.86 Hz	**Mode 4**	f_4 = 677.47 Hz

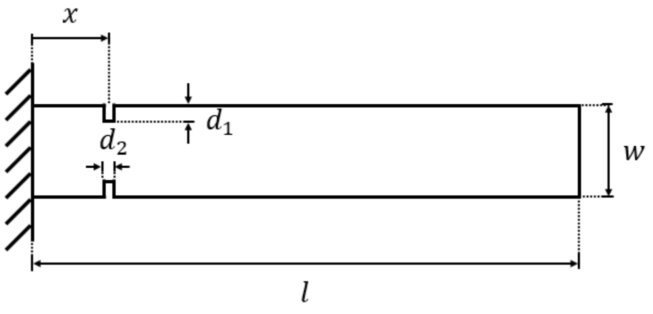

Figure 1. Top view representation of the fixed-free beam.

for each mode, the resulting RNFC surfaces can be used to identify both the location and depth of the damage.

2.2. Eigensystem realization algorithm

Eigensystem Realization Algorithm (ERA) is a realization method used to identify a state-space model by analyzing the system's response to an impulse excitation, developed by (Juang & Pappa, 1985). In the Eq. (2), discrete state-space representation of the system is given, where $x \in \mathcal{R}^{r\times1}$ denotes the state vector, and *r* is the number of states; $y \in \mathcal{R}^{p\times1}$ is the output vector with *p* outputs; and $u \in \mathcal{R}^{m\times1}$ represents the input vector with *m* inputs. *A*, *B*, *C*, and *D* are state, input, output, and feedthrough matrices, respectively.

$$\begin{aligned} x(t+1) &= Ax(t) + Bu(t) \\ y(t) &= Cx(t) + Du(t) \end{aligned} \tag{2}$$

In a discrete-time representation, impulse excitation to a stationary system can be modelled using Dirac's delta function, where the input is zero at all times except at *t=0*, as shown in Eq. (3).

$$\begin{aligned} x(t=0) &= 0 \\ x(t\neq0) &\neq 0 \\ u(t=0) &\neq 0 \\ u(t\neq0) &= 0 \end{aligned} \tag{3}$$

By applying impulse excitation defined in Eq. (3), in Eq. (2) the response of the system can be obtained in terms of state matrices as given in Eq. (4). In the equation G_t is Markov Parameters.

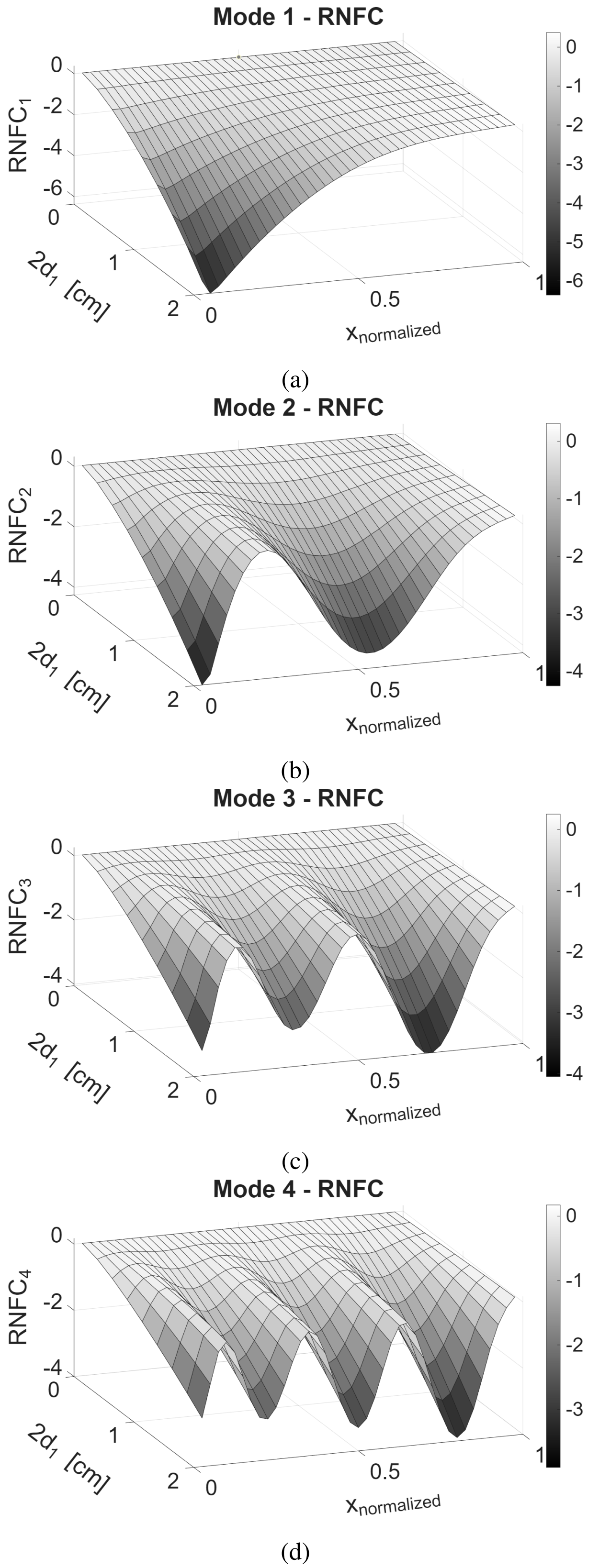

Figure 2. RNFC surfaces for the first four modes, (a)-Mode 1, (b)-Mode 2, (c)-Mode 3, and (d)-Mode 4.

$$y\left(t\right) = G_t u(0) = \begin{cases} Du\left(0\right), & t = 0 \\ CA^{t-1}Bu\left(0\right), & t \neq 0 \end{cases} \tag{4}$$

By dividing the system's response by the magnitude of the impulse, the Markov parameters can be obtained and subsequently used to construct the Hankel matrix, as shown in Eq. (5). It should be noted that the excitation generated by an impact hammer closely resembles, but is not exactly, an ideal impulse. The nonzero duration of the force depends on the stiffness of the structure under investigation and the tip material of the impact hammer. To accurately derive the Markov parameters, the time integral of the measured excitation must be computed. Considering that a discrete impulse with $u(t = 0) = 1$ has a time integral equal to the sampling interval $\triangle t$, an appropriate normalization should be applied to ensure the correct estimation of the Markov parameters.

$$H_1 = \begin{bmatrix} G_1 & G_2 & \dots & G_n \\ G_2 & G_3 & \dots & G_{n+1} \\ \vdots & \vdots & \ddots & \vdots \\ G_k & G_{k+1} & \dots & G_{n+k-1} \end{bmatrix} \tag{5}$$

The Hankel matrix can also be explicitly defined using the Eq. (4) as shown in the Eq. (6), in terms of state matrices.

$$H_1 = \begin{bmatrix} CB & CAB & \dots & CA^{n-1}B \\ CAB & CA^2B & \dots & CA^nB \\ \vdots & \vdots & \ddots & \vdots \\ CA^{k-1}B & CA^kB & \dots & CA^{n+k-2}B \end{bmatrix} \tag{6}$$

The explicitly defined Hankel matrix is the product of the extended observability matrix -$\mathcal{O}_k$- ,and the extended controllability matrix -$\mathcal{C}_n$- as given in the Eq. (7). Therefore, by decomposing Hankel matrix, both observability and controllability matrices can be obtained.

$$H_1 = \begin{bmatrix} C \\ CA \\ \vdots \\ CA^{k-1} \end{bmatrix} \begin{bmatrix} B & AB & \dots & A^{n-1}B \end{bmatrix} = \mathcal{O}_k\mathcal{C}_n \tag{7}$$

Decomposition can be performed using Singular Value Decomposition (SVD) by retaining only the most important singular values and their corresponding singular left and right vectors as shown in the Eq. (8). In the equation, Σ is a diagonal matrix containing singular values, while U and V are the matrices containing the left and right singular vectors, respectively. This truncation, denoted with subscript 1, enables the identification of a reduced-order system that captures the dominant dynamics of the system. Since only the first four modes are investigated in the study, the first eight singular values and their associated vectors have been used.

$$H_1 = U\Sigma V^T = \begin{bmatrix} U_1 & U_2 \end{bmatrix} \begin{bmatrix} \Sigma_1 & 0 \\ 0 & 0 \end{bmatrix} \begin{bmatrix} {V_1}^T \\ {V_2}^T \end{bmatrix} = U_1\Sigma_1{V_1}^T \tag{8}$$

Considering two decomposed Hankel matrix provided in the Eq. (7) and Eq. (8), the relationship between SVD results and observability and controllability matrices can be established, as shown the Eq. (9).

$$H_1 = \mathcal{O}_k\mathcal{C}_n = U_1\sqrt{\Sigma_1}\sqrt{\Sigma_1}{V_1}^T \tag{9}$$

Since the singular vectors obtained from SVD are unitary, a balanced realization can be achieved by further decomposing Σ_1 through its square root as given in the Eq. (10).

$$\begin{aligned} \mathcal{O}_k &= U_1\sqrt{\Sigma_1} \\ \mathcal{C}_n &= \sqrt{\Sigma_1}{V_1}^T \end{aligned} \tag{10}$$

By using the appropriate sections of the observability and controllability matrices -specifically, the first four rows of the observability matrix corresponding to the four piezoelectric sensors, and the first column of the controllability matrix corresponding to the single impact hammer input— as shown in Eq. (7), the state-space matrices *B*, and *C* can be obtained. To compute the *A* matrix, a time shifted Hankel Matrix denoted as H_2 should be constructed as given in Eq. (11).

$$H_2 = \begin{bmatrix} G_2 & G_3 & \dots & G_{n+1} \\ G_3 & G_4 & \dots & G_{n+2} \\ \vdots & \vdots & \ddots & \vdots \\ G_{k+1} & G_{k+2} & \dots & G_{n+k} \end{bmatrix} \tag{11}$$

The time shifted Hankel matrix can also be explicitly defined using the same formulation provided in Eq. (4), as shown in the Eq. (12), in terms of state matrices.

$$H_2 = \begin{bmatrix} CAB & CA^2B & \dots & CA^nB \\ CA^2B & CA^3B & \dots & CA^{n+1}B \\ \vdots & \vdots & \ddots & \vdots \\ CA^kB & CA^{k+1}B & \dots & CA^{n+k-1}B \end{bmatrix} \tag{12}$$

It can be seen that time shifted Hankel matrix is actually the product of the observability matrix, the state matrix *A*, and the controllability matrices. By using the observability and controllability matrices obtained from the original Hankel matrix, the time shifted Hankel matrix can be defined as given in Eq. (13).

$$H_2 = \mathcal{O}_k A \mathcal{C}_n = U_1 \sqrt{\Sigma_1} A \sqrt{\Sigma_1} {V_1}^T \tag{13}$$

Since SVD produces orthonormal vectors, the inverse of the right and left singular vector matrices can be represented by their transposes. Considering this property, the state matrix A can be formulated as shown in Eq. (14).

$$A = (\sqrt{\Sigma_1})^{-1} {U_1}^T H_2 V_1 (\sqrt{\Sigma_1})^{-1} \tag{14}$$

By converting the state-space model into its modal form, the natural frequencies of the beam can be determined. By implementing RNFC formulation given in the Eq. (1), the frequency shifts due to damage can be quantified from the experimental results.

2.3. Nearest neighbor algorithm

The experimental RNFC values obtained from the ERA are compared with the RNFC surfaces derived from numerical analyses. Using the NN algoritm, the most likely damage parameters that lead to experimentally observed frequency shift can be predicted. For each damage scenario, the numerical RNFC values of the first four modes are combined into a vector, and the Euclidean distance between these vectors and the experimental RNFC vector are calculated, as shown in Eq. (15). The numerical model with the smallest distance to the experimental data is selected as the closest match.

$$d_{euclidean} = \sqrt{\sum_{i=1}^{4} (RNFC_{iExp.} - RNFC_{iFEA})^2} \tag{15}$$

3. EXPERIMENTAL SETUP

The experimental setup for the fixed-free beam is shown in Figure 3. The fixed end of the CFRP beam is clamped to the optical table, and the excitation is applied using an impact hammer at a point near the fixed end, as illustrated in the figure. The dynamic response of the beam is measured using both a laser vibrometer and piezoelectric sensors. The laser vibrometer is employed to validate the measurements from the piezoelectric sensors.

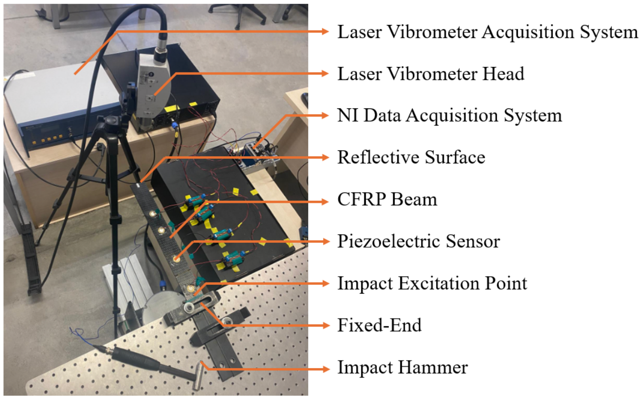

Figure 3. Experimental setup.

Table 4. β_n values.

β_n values			
$\beta_1 l$	1.8751	$\beta_3 l$	7.8548
$\beta_2 l$	4.6941	$\beta_4 l$	10.996

3.1. Sensor locations

The sensor locations are determined based on the theoretical mode shapes and mode curvatures of the fixed-free beam. The mode shape corresponding to the n^{th} vibrational mode is given in Eq. (16) as described by (Rao, 2019), where W_n denotes the mode shape and n refers to the mode number. In the equation β_n is a constant associated with the n^{th} mode, and its numerical values are provided in Table 4. For the laser vibrometer, the measurement is performed at the free end of the beam, as it exhibits nonzero deflection for all vibration modes.

However, since piezoelectric sensors generate electrical charge in response to mechanical deformation, the mode curvatures are analyzed to identify points with nonzero curvature—indicating the presence of internal moment and strain— ensuring optimal sensor placement. The mode curvature can be defined by taking second derivative of the Eq. (16) with respect to x, and the result can be seen in the Eq. (17).

A graphical representation of the mode shapes and corresponding mode curvatures is provided in Figure 4, where $x = 0$ denotes the fixed end. In the figure, zones where the curvature magnitude is below 10 % of the maximum are indicated and avoided when placing piezoelectric sensors. The final sensor locations, as well as the excitation points, are also illustrated in the figure, details of the sensor locations are given in Table (5).

Table 5. Sensor placements.

Sensor and Excitation Points			
Piezoelect. Sens. 1	0.075L	Piezoelect. Sens. 3	0.55L
Piezoelect. Sens. 2	0.3L	Piezoelect. Sens. 4	0.7L
Excitation point	0.0375L		

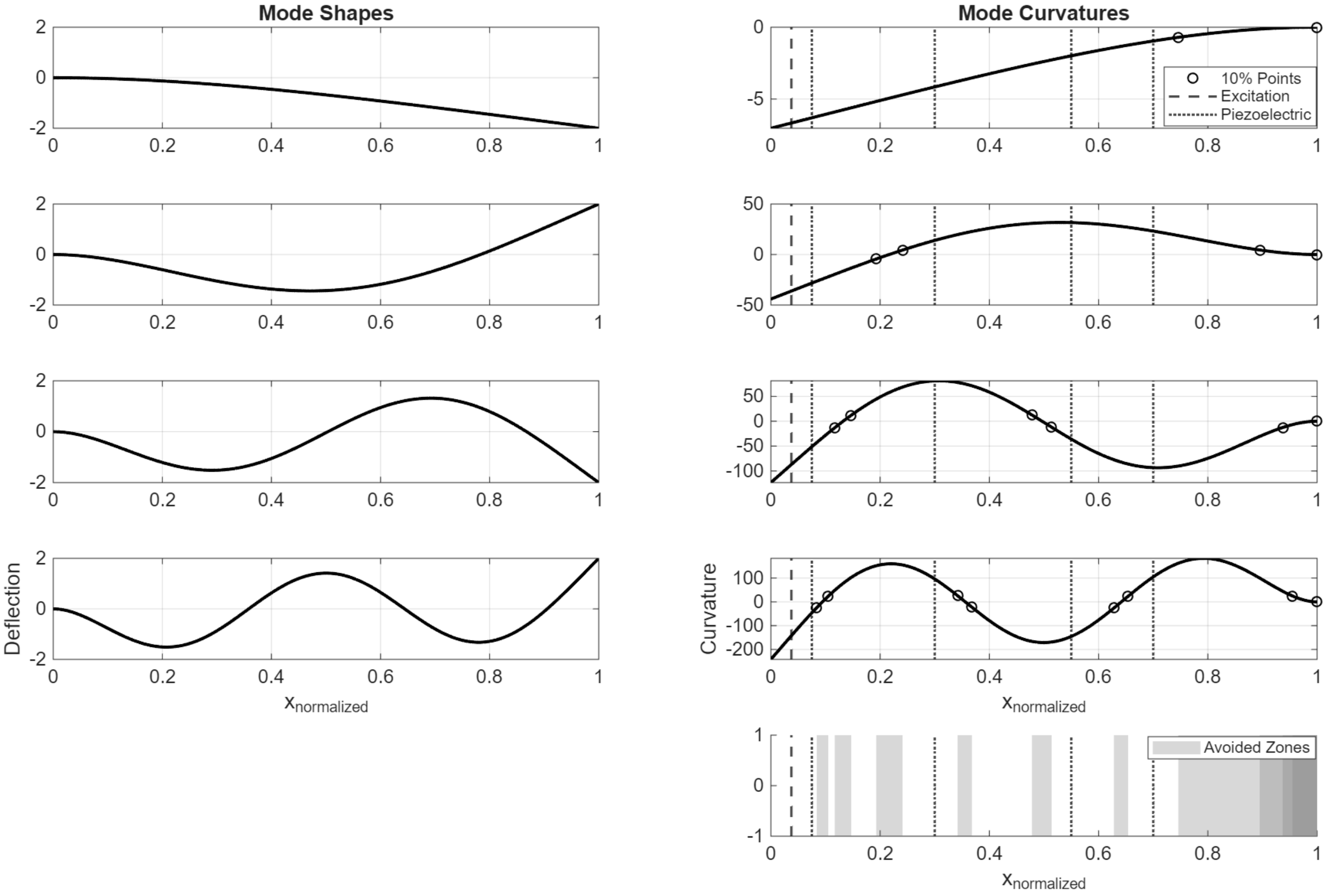

Figure 4. Mode shapes and Mode Curvature for the first four modes, and avoided zones.

$$W_n(x) = (\cos(\beta_n x) - \cosh(\beta_n x)) - \frac{\cos(\beta_n l) + \cosh(\beta_n l)}{\sin(\beta_n l) + \sinh(\beta_n l)} (\sin(\beta_n x) - \sinh(\beta_n x)) \tag{16}$$

$$\frac{d^2 W_n(x)}{dx^2} = \beta_n^2\big(-\cos(\beta_n x) - \cosh(\beta_n x)\big) - \frac{\cos(\beta_n l) + \cosh(\beta_n l)}{\sin(\beta_n l) + \sinh(\beta_n l)}\, \beta_n^2\big(-\sin(\beta_n x) - \sinh(\beta_n x)\big) \tag{17}$$

3.2. Experimental cases

To validate the model, three damage scenarios were experimentally investigated. In the first case, a single damage was introduced 8 cm from the fixed end of the beam, with a depth of 1 cm. In the second case, the damage depth at the same location was increased to 2 cm. Finally, in the third case, an additional damage was introduced 14 cm from the fixed end with a depth of 1 cm. These scenarios are summarized in Table (6), and the pictures of the corresponding damage cases are provided in Figure (5). Subfigures *(a)*, *(b)*, and *(c)* correspond to *Case 1*, *Case 2*, and *Case 3*, respectively.

Table 6. Damage cases.

	Damage Position	Damage Depth ($2d_1$)
Case 1	8 cm (0.2L)	1 cm
Case 2	8 cm (0.2L)	2 cm
Case 3	8 cm (0.2L) 14 cm (0.35L)	2 cm 1 cm

4. RESULTS AND DISCUSSION

For the intact specimen and each of the three damage cases, nine measurements were performed per case. The corresponding average results are summarized in Table (7), where the notation ± indicates the sample standard deviation associated with each measurement set. In the table, the extracted modal parameters- specifically, natural frequencies and damping ratios- corresponding to the first four vibration modes are provided. It should be noted that the measured natural frequencies of the intact specimen differ from the numerical results by approximately 10%. This discrepancy may be attributed to challenges in achieving a perfectly fixed bound-

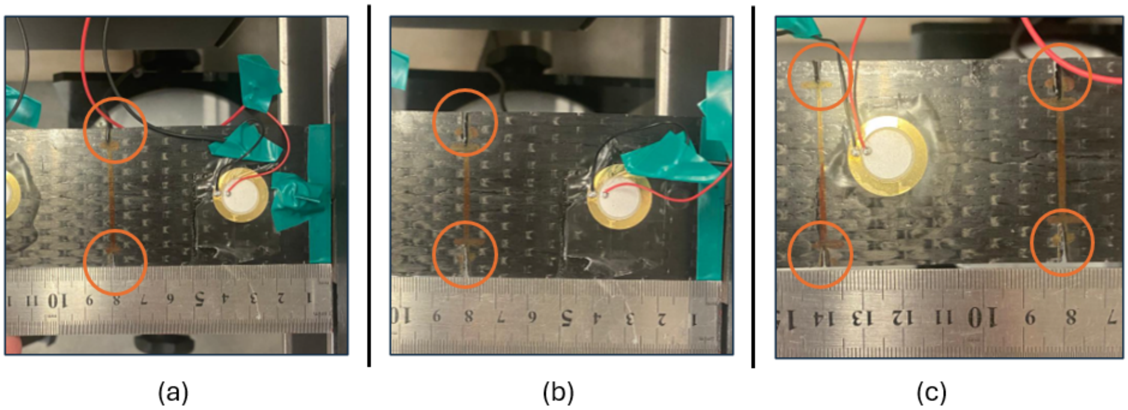

Figure 5. Photographs of the damages, (a)-Case 1, (b)-Case 2, and (c)-Case 3.

Table 7. ERA results.

	Mode 1	Mode 2	Mode 3	Mode 4
	f_1 *(Hz)*	f_2 *(Hz)*	f_3 *(Hz)*	f_4 *(Hz)*
Intact	17.9629 ± 0.0067	114.231 ± 0.019	320.826 ± 0.034	628.298 ± 0.028
Case 1	17.7845 ± 0.0068	114.380 ± 0.045	319.262 ± 0.058	622.423 ± 0.067
Case 2	17.2351 ± 0.0154	114.032 ± 0.038	314.888 ± 0.101	609.887 ± 0.090
Case 3	17.1131 ± 0.0032	113.253 ± 0.031	312.964 ± 0.123	609.648 ± 0.079
	ζ_1 $(*10^{-3})$	ζ_2 $(*10^{-3})$	ζ_3 $(*10^{-3})$	ζ_4 $(*10^{-3})$
Intact	3.873 ± 0.158	5.019 ± 0.387	3.307 ± 0.050	3.777 ± 0.033
Case 1	3.684 ± 0.106	12.841 ± 0.964	4.336 ± 0.564	4.108 ± 0.091
Case 2	4.359 ± 0.414	9.437 ± 0.678	4.184 ± 0.371	3.663 ± 0.030
Case 3	3.852 ± 0.185	5.715 ± 0.195	4.494 ± 0.167	3.674 ± 0.072

ary condition in the experimental setup, as well as the potential presence of voids within the matrix of the composite.

The results indicate that the percentage of the standard deviation relative to the mean of the measurements, for natural frequencies does not exceed 0.09%, suggesting that both the experimental procedure and the ERA formulation yield consistent and reliable results.

Using the mean value of the measured natural frequencies, the experimental frequency shifts are quantified based on the RNFC formulation presented in the Eq. (1). The corresponding RNFC results are summarized in Table (8). It should be noted that for *Case 3*, the objective is to identify the additional damage located at 14 cm from the fixed end, given that a damage is already known at 8 cm away from the fixed end. Assuming linear superposition of damage effects, the RNFC values for *Case 3* are calculated relative to the *Case 2*.

Table 8. Experimental RNFC results.

	$RNFC_1$	$RNFC_2$	$RNFC_3$	$RNFC_4$
Case 1	-0.9936	0.1307	-0.4875	-0.9351
Case 2	-4.0518	-0.1742	-1.8506	-2.9303
Case 3	-0.6789	-0.6813	-0.6000	-0.0381

As shown in Table (8), introduced damages affect each vibration mode differently, as expected. For instance, the damage located 8 cm from the fixed-end in *Case 1* and *Case 2* has a relatively minor effect on the second mode compared to the other three modes. This is because the damage is positioned near a nodal point of the second mode's curvature shape (at a normalized position of *x=0.2*), as indicated in Figure (4). At this location, the internal moment is close to zero, meaning the removed material contributes minimally to the bending stiffness associated with second mode.

In fact, the damage in *Case 1* results in a slight increase in the second natural frequency compared to the intact case—an outcome that is not typically expected. However, for damage parameter prediction, the frequency shifts of all four modes are used in combination with the NN algorithm. By leveraging information from multiple modes, the influence of individual anomaly is reduced, thereby improving the robustness and reliability of the prediction.

The results of the NN algorithm, based on FEA-generated RNFC surfaces and experimental RNFC values, are presented in Table (9). The algorithm predicted the damage location in all three cases with a maximum error of 1 cm, corresponding to 2.5% of the total beam length (40 cm), as defined in

Table 9. Nearest Neighbor algorithm predictions.

	Actual		Prediction		Percent Error (%)	
	Loc.	Depth	Loc.	Depth	Loc.	Depth
Case 1	8 cm	1 cm	9 cm	1 cm	2.5	0
Case 2	8 cm	2 cm	9 cm	2 cm	2.5	0
Case 3	14 cm	1 cm	15 cm	1 cm	2.5	0

the Eq. (18), where *PE* denotes the percent error. The severity of the damage was predicted without error, demonstrating the effectiveness of the proposed approach. By considering *k* closest predictions, it is possible to estimate a broader damage zone, providing insight into the region experiencing stiffness reduction.

$$PE = \left| \frac{x_{actual} - x_{prediction}}{l} \right| \times 100\% \qquad (18)$$

Figure (6) compares the RNFC values and prediction results with the FEA-based RNFC surfaces. The figure confirms the consistency between experimental and model data, supporting the accuracy of the proposed damage identification method.

5. CONCLUSION

This study aimed to identify the location and severity of damage in a CFRP beam using vibration-based measurements, supported by numerical results obtained through FEA. The damage-induced natural frequency shifts were quantified using the RNFC formulation. Based on this, RNFC surfaces were constructed for the first four vibrational modes, capturing their dependence on both damage location and severity.

Since each mode is affected differently by the damage characteristics, the RNFC surfaces were used for inverse analysis. The experimentally measured time domain data investigated using ERA, a reduced order subspace system identification method. The extracted modal parameters are used to quantify RNFC results of the experiments. NN algorithm is then employed to find the closest matching damage scenario, thereby estimating the most likely damage parameters.

The applied method predicted the damage location within 1 cm for a 40 cm beam, corresponding to 2.5% error, and damage depth predicted accurately. However, it should be noted that the investigated damage depths (1 cm and 2 cm) are relatively large compared to the beam width (5 cm). The accuracy of the method should be further investigated with subtle damage cases, which may correspond delamination defects. Additionally, for future work, the method will be investigated for plate-like or more complex three-dimensional structures, and its assessment capability will be evaluated.

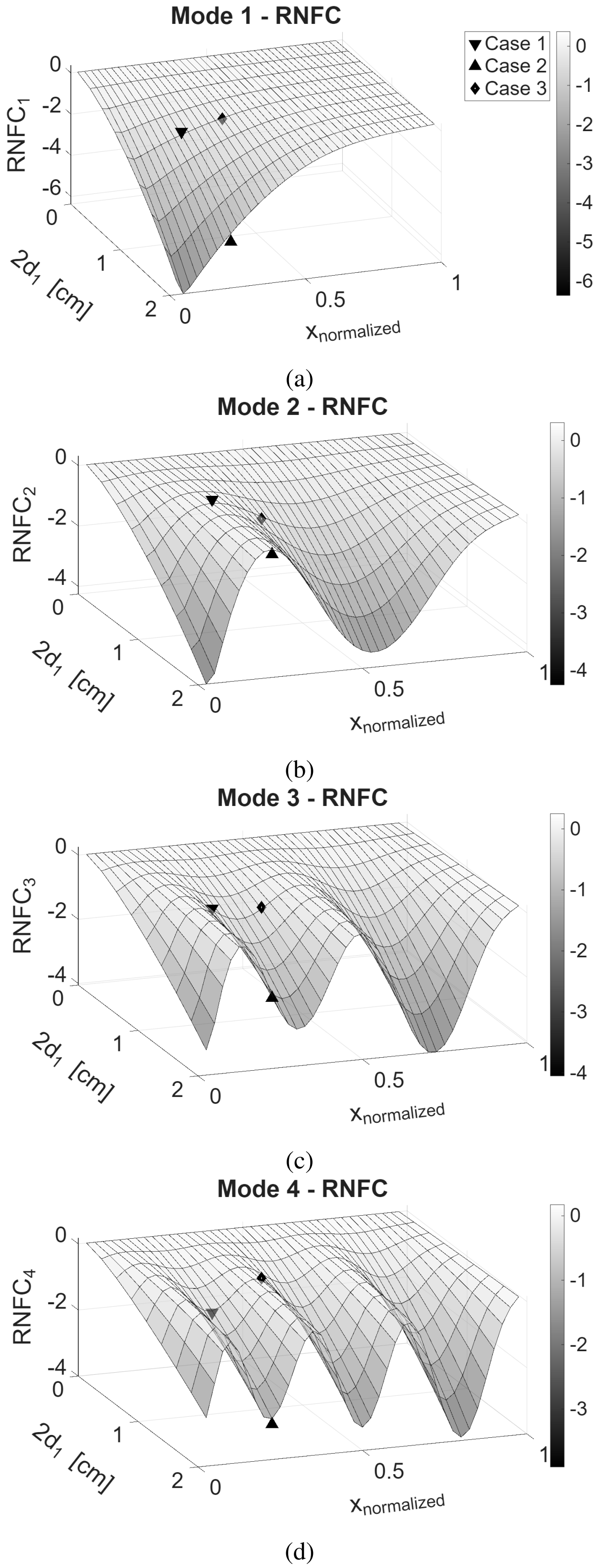

Figure 6. Prediction results.

ACKNOWLEDGMENT

This study is funded by TUBITAK (The Scientific and Technological Research Council of Turkey) through project grant no 123M891.

REFERENCES

Abasi, A., Harsij, V., & Soraghi, A. (2021). Damage detection of 3d structures using nearest neighbor search method. *Earthquake Engineering and Engineering Vibration*, *20*(3), 705–725.

Dahak, M., Touat, N., & Kharoubi, M. (2019). Damage detection in beam through change in measured frequency and undamaged curvature mode shape. *Inverse Problems in Science and Engineering*, *27*(1), 89–114.

Gillich, G.-R., & Praisach, Z.-I. (2014). Modal identification and damage detection in beam-like structures using the power spectrum and time–frequency analysis. *Signal Processing*, *96*, 29–44.

Juang, J.-N., & Pappa, R. S. (1985). An eigensystem realization algorithm for modal parameter identification and model reduction. *Journal of guidance, control, and dynamics*, *8*(5), 620–627.

Kaw, A. K. (2005). *Mechanics of composite materials*. CRC press.

Rao, S. S. (2019). *Vibration of continuous systems*. John Wiley & Sons.

Sause, M. G., & Jasiūnienė, E. (2021). *Structural health monitoring damage detection systems for aerospace*. Springer Nature.

Sha, G., Radzieński, M., Cao, M., & Ostachowicz, W. (2019). A novel method for single and multiple damage detection in beams using relative natural frequency changes. *Mechanical Systems and Signal Processing*, *132*, 335–352.

Yan, Y., Cheng, L., Wu, Z., & Yam, L. (2007). Development in vibration-based structural damage detection technique. *Mechanical systems and signal processing*, *21*(5), 2198–2211.

Zhang, Z., Shankar, K., Ray, T., Morozov, E. V., & Tahtali, M. (2013). Vibration-based inverse algorithms for detection of delamination in composites. *Composite Structures*, *102*, 226–236.